Available online at www.sciencedirect.com
SCIENCE DIRECT®
Journal of Colloid and Interface Science 276 (2004) 439–449
JOURNAL OF Colloid and Interface Science
www.elsevier.com/locate/jcis

Foam drainage on the microscale II. Imaging flow through single Plateau borders

S.A. Koehler [a,*], S. Hilgenfeldt [b], E.R. Weeks [a], H.A. Stone [c]

[a] *Physics Department, Emory University, Atlanta, GA 303022, USA*
[b] *Faculty of Applied Physics, University of Twente, P.O. Box 217, 7500 AE Enschede, The Netherlands*
[c] *Division of Engineering and Applied Sciences, Harvard University, Cambridge, MA 02138, USA*

Received 14 July 2003; accepted 19 December 2003

Available online 24 June 2004

Abstract

The liquid in foam forms an interconnected network, which is composed of Plateau borders, nodes, and films. One of the dominant pathways for foam drainage is flow through Plateau borders, and we use confocal microscopy to obtain experimental results for the flow fields inside individual Plateau borders. For three types of surfactants detailed comparisons are made with a model based upon the influence of surface viscosity at free boundaries between the gas in the bubbles and the liquid in the Plateau borders. The model describes the flows well, and we find good agreement between the surface viscosity predicted by this model and representative values found in the literature. We also give a qualitative description of the flow in the nodes.

Keywords: Foams; Emulsions; Surface rheology

1. Introduction

Foam drainage is the flow of liquid between the bubbles that make up the foam, and generally the driving forces are gravity and capillarity. Liquid flows through an interconnected network that consists of channels, also known as Plateau borders, where the flow essentially is unidirectional, and nodes, which are the junctions of four channels. Early foam drainage experiments dealt with the foam fractionation process, which is used to remove surfactants from solution [1–3]. Another question that received attention, was the drainage of free-standing foams due to the influence of gravity [4–6]. Later, an elegant experiment called forced (foam) drainage was developed and modeled, where a continuous pulse of liquid injected into a foam produced a traveling wave [7,8]. A variant of this experiment is pulsed drainage, where a small finite pulse of liquid is injected into the foam, and the spreading of the pulse has been investigated in one and two dimensions [9–11]. The influence of variations in the cross-section of the foam container on the drainage rates has been investigated as well [12,13]. In all of the above cases, the drainage experiments were conducted on the macroscopic level, where the length scale was large compared to the bubble size, i.e., on the scale of centimeters. This is far larger than the length scale relevant to the fluid flow in individual channels, whose widths typically are on the order of tens of micrometers.

Foam drainage is a complicated process that is not fully understood, and several different mean-field models have been proposed to describe motion on the macroscale of many bubbles. All foam drainage models, however, are based upon consideration of the flow on the microscale, i.e., on the scale of individual channels and nodes. These results are then suitably averaged to develop a macroscopic foam drainage model, which is used for comparison with macroscopic experiments. The major differences in the models are solely due to the details of the microscopic assumptions, because the averaging procedure to arrive at a macroscopic description from the microscopic model generally is agreed upon. Therefore detailed microscopic measurements are necessary to make further progress both in the microscopic and macroscopic understanding of foam drainage.

* Corresponding author.
E-mail address: skoehler@physics.emory.edu (S.A. Koehler).
URL: http://www.physics.emory.edu/faculty/koehler.

0021-9797/$ – see front matter
doi:10.1016/j.jcis.2003.12.060

In this work we will present results obtained from a new technique that visualizes the flow through the foams within individual channels [14]. These experiments have revealed that the flow through individual channels depends on the type of surfactant used to create the foam. A variety of different surfactants are investigated and we offer interpretations based upon a model with a liquid/gas interface that has Newtonian surface viscosity. For channels the flow is unidirectional, and therefore relatively straightforward to model. In contrast, the flow in the nodes is more complicated, because the node is the junction of four channels. Not only is the modeling more complicated, but experimentally mapping out the microscopic flow fields is far more difficult as well. Thus we present only qualitative new results for the nature of the flow through the nodes.

2. Experimental procedure

We determined the velocity fields for forced drainage on the scale of individual Plateau borders using confocal microscopy [14]. Rather than tracking the velocity of the forced drainage wave on the scale of several centimeters, as had been done traditionally, we tracked the motion of tracer particles flowing through the liquid network on the scale of micrometers.

We used a ThermoNoran Oz confocal microscope, which is based upon an acousto-optical device, and therefore was sufficiently fast to take movies at ∼100 frames/s and track particle velocities up to ∼1 mm/s. The main advantage of confocal microscopy is that it uses a spatial filtering technique to achieve thin optical sections deep within the sample. The tracer particles were fluorescent latex spheres, with a diameter of one micrometer, and present in the surfactant solution at a volume fraction of about 10^{-6}. This suspension was continuously injected into the foam a few centimeters above the field of view. Only at low liquid volume fractions, $\epsilon \lesssim 10^{-2}$, is the foam sufficiently transparent to enable imaging interior channels with the confocal microscope setup. Imaging analysis software developed for tracking colloidal particles was used to determine the flow field [15]. Once the particles within the movie had been identified and located, the velocity field was determined by taking the differences in the positions of the particles from frame to frame.

We imaged the flow fields of aqueous foams made with different types of surfactant solutions: a protein solution, an ionic soap, and a nonionic soap. The protein foam was made with bovine serum albumin (BSA) and the cosurfactant propylene glycol alginate (to improve the foam stability [16]) at a concentration of about 4 g/l each in a pH 4 acetic acid buffer solution. A second foam was stabilized with sodium dodecyl sulfate (SDS), which is an ionic surfactant and found in many common soaps. A third foam was made with Tween 20, which is a nonionic surfactant. For the SDS and Tween 20 foams, the concentration of surfactant

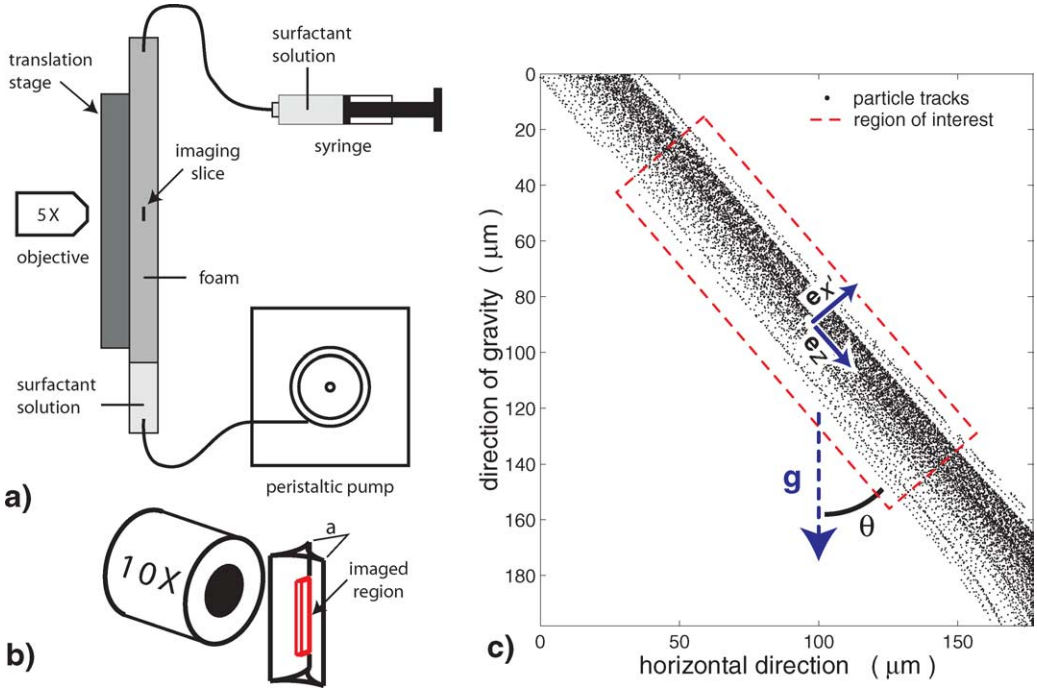

Fig. 1. Details of the confocal imaging of the flow profiles within a single channel inside a foam. (a) Schematic of the experiment. The microscope is tipped sideways with the foaming tube attached to the translation stage. A syringe is used to perfuse the foam with the solution from the top, and the foam is created by injecting gas into the bottom by a peristaltic pump. (b) A close-up schematic of the objective that images a small parallelepiped region within the channel. (c) The traces captured by the confocal microscope of the particles flowing through an interior channel of a Tween 20 foam, which is inclined $\theta = 41°$ to the vertical. The flow direction of the liquid in the channel is indicated by the solid arrow $\mathbf{e}_z$, and the direction transverse to the flow is indicated by the solid arrow $\mathbf{e}_{x'}$.

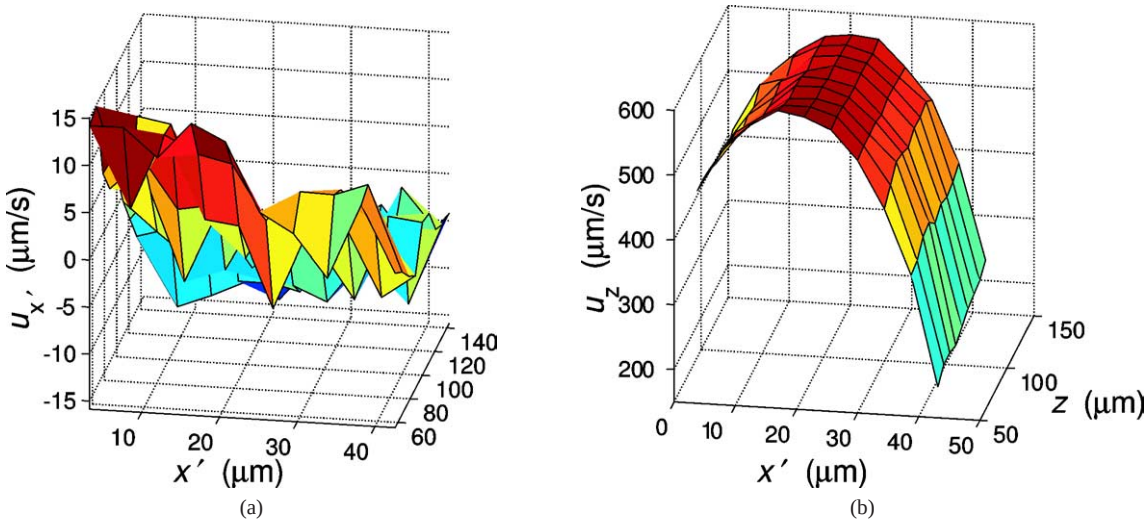

Fig. 2. The flow field of an axial slice down an interior channel from an SDS foam, with orientation $\theta \approx 58°$. (a) The flow field of the transverse velocity, $u_{x'}$, is plotted in the $x' \times z$ plane. (b) The axial velocities, u_z, are plotted in the $x' \times z$ plane. Note that the axial velocities are considerably larger than the transverse velocities, and the axial velocities at the channel edges are comparable in magnitude to the maximum velocity.

was approximately 1 g/l. The bulk viscosity of the protein solution was $\mu \approx 0.07$ g/cm/s and that of the soap solutions was $\mu \approx 0.01$ g/cm/s. Air was introduced into the bottom of the solution through a syringe needle, which produced bubbles about 3 mm in diameter. Typically the channel widths were $a \approx 100$ μm, and the channel lengths were $L \approx 1$ mm, so that the liquid volume fraction was $\epsilon \approx 10^{-3}$. This is small compared to conventional foam drainage experiments, where the liquid volume fractions usually span the range $10^{-3} \lesssim \epsilon \lesssim 10^{-1}$. We obtained over a dozen good velocity fields altogether for exterior (i.e., channels that contact a container wall) and interior channels of three types of foams.

Fig. 1 schematically shows the details of imaging the microscopic flow profiles in foams. Since the flow is driven by gravity, the general flow direction is downward, and we rotated the microscope onto its side so that the imaging slice was oriented vertically as well, as shown schematically in Fig. 1a. The foaming tube is attached to the microscope's translation stage, air is injected via a peristaltic pump from the bottom, and the same surfactant solution with the fluorescent latex particles is injected above the microscope's field of view using a digital syringe pump. The experiments were all performed under steady drainage. Typically we used low-magnification objectives, such as 10×, with a field of view of about 250 × 250 μm. We estimate that the depth of the confocal imaging slice is about 10 μm. In Fig. 1b, a sketch of the objective lens, which images a small parallelepiped region inside the channel, is shown. Most of the interior channels have orientations incommensurate with that of the confocal imaging slice, making it necessary to search for channels that lie within the confocal slice. Locating interior channels, which were at least one bubble radius away from the walls and suitably aligned with the vertical confocal imaging slice, required patient searching. On the other hand exterior channels already are properly aligned for imaging, because they are contacting the container wall.

Fig. 1c shows the traces of the particles moving through a region of the channel in about 1 s for an interior channel that is aligned at an angle $\theta \approx 41°$ with the vertical. In the lower right-hand corner of the figure the channel flares out and outside the plot's field of view the channel joins with three other channels to form a node. We shall denote the channel's direction by $\mathbf{e}_z$ and the direction transverse to the channel in the confocal plane by $\mathbf{e}_{x'}$.

3. Experimental results

The particle velocities were measured in a parallelepiped region given by the intersection of the imaging slice and a channel. Two components of the velocity fields are imaged: along the direction of the channel, u_z, and transverse to the direction of the channel in the plane of the confocal slice, $u_{x'}$ (see Fig. 1c).

We determined the velocity profiles using a straightforward procedure. The region of interest in the channel, indicated by the box with dashed lines in Fig. 1c, is divided into $N \approx 10$ evenly spaced bins in the transverse direction, and the average axial and transverse velocities for each bin are determined [17]. For the purposes of modeling we assume that the particles are uniformly distributed in each bin.

Figs. 2 and 3 show slices of the velocity fields of interior channels from SDS and protein foams, respectively. Because each channel is randomly oriented, it is highly unlikely that the edges of the channel are within the imaging slice. We need to introduce a coordinate system $x' \times y' \times z$ for each confocal image of a channel, where $\mathbf{e}_z$ is along the direction of the flow, $\mathbf{e}_{x'}$ is transverse to the flow in the imaging

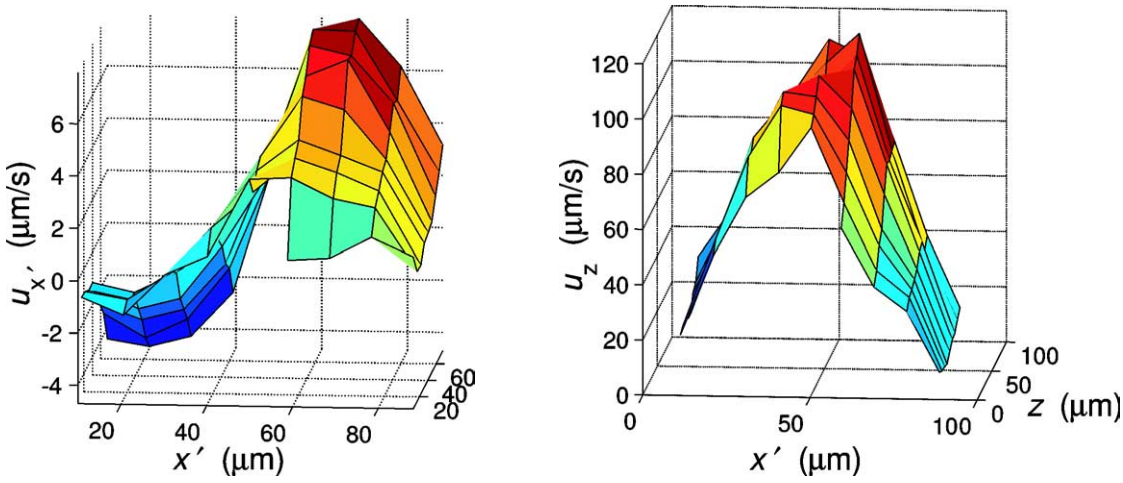

Fig. 3. The flow field inside an interior BSA channel, with orientation $\theta \approx 75°$. (a) The flow field of the transverse velocity, $u_{x'}$, is plotted in the $x' \times z$ plane. (b) The axial velocity field, u_z, is plotted in the $x' \times z$ plane; notice that here the velocities at the channel edges are small compared to the maximum velocity.

plane and $\mathbf{e}_{y'}$ is normal to the confocal slice. (This choice of axes is dictated by the imaged channel's orientation and is distinct from the more natural choice of axes $x \times y \times z$ used for modeling in [18].) The velocities do not vary significantly along the z-direction, which is expected because the channels are long and slender and do not vary much in cross-sectional area. Comparing Figs. 2a with 2b and 3a with 3b shows that the transverse velocities, $u_{x'}$, are considerably smaller than the axial velocities, u_z. The small transverse velocities may be attributed to slight variations in the channel's cross-section or a slight mismatch between our choice for the z-direction and the actual direction of flow through the channel.

In Figs. 2 and 3, respectively, the apparent width of the SDS channel is about 50 μm, and for the protein channel the apparent width is about 80 μm. The actual width, a, is wider than the width apparent from the figures; however, directly measuring a was not possible, because we do not know the channel's orientation relative to the objective lens, nor can we reliably determine the boundaries of a channel. Although the confocal movies only lasted for a few seconds each, there was about a minute of downtime between movies, and on this time scale the foam geometry subtly changed due to coarsening. So taking movies from different slices of the same channel at different depths to obtain more information about the geometry was not feasible.

There are two significant differences between the SDS and BSA velocity profiles. The first is that although the apparent width of the BSA channel is greater, which suggests a larger liquid volume fraction and hence faster flow velocities, the BSA axial velocities are considerably slower than the SDS velocities. The second striking difference is that at the edges of the BSA channel, the velocities are small, about 10 μm/s, whereas for the SDS channel the edge velocity is considerably higher, on the order of 100 μm/s. This indicates that the interfaces of SDS foams are highly mobile, with interfacial velocities about half the maximal velocity (we find similar results for Tween 20 foams). On the other hand, the interfacial velocities of protein channels are low compared to their maximal velocities.

Because flow in the nodes is not unidirectional, visualizing and describing the flow is more complicated than the flow in the channels. We consider an interior BSA node whose velocity field is shown in Figs. 4a and 4b. The flow starts at $z < 0$, moves downward in the direction of increasing z, and branches out in the node region that starts at $z \approx 50$ μm. The velocity along the z direction, u_z, is shown in Fig. 4a, the velocity profile in the channel is parabolic and it is apparent that, in the node region, u_z has diminished. Initially $u_{x'}$ is small (see Fig. 4b) and it increases as the flow is redirected in the node region. Most importantly, the velocity gradients in the nodes are clearly occurring on the scale of the channel width a.

4. Analysis of the experimental data

4.1. Flow in channels

Here we summarize a model [14] based on the ideas originally introduced by Leonard and Lemlich [2] for flow along the length of a realistically shaped Plateau border, with an interface having a Newtonian surface viscosity, μ_s. The typical radius of curvature of the channel is denoted by a, and the shear viscosity of the bulk liquid is denoted by μ. Where the channel contacts either a film or the container wall a Dirichlet velocity boundary condition is assumed (i.e., the axial velocity $u_z = 0$). This boundary condition is based upon observations of the circulatory flow in the films, which is upwards at the edges and downwards in the middle. Since the velocity in the channels is downwards and the velocity field is continuous, there is a region between the channel and the edge of the film where the velocity must be zero.

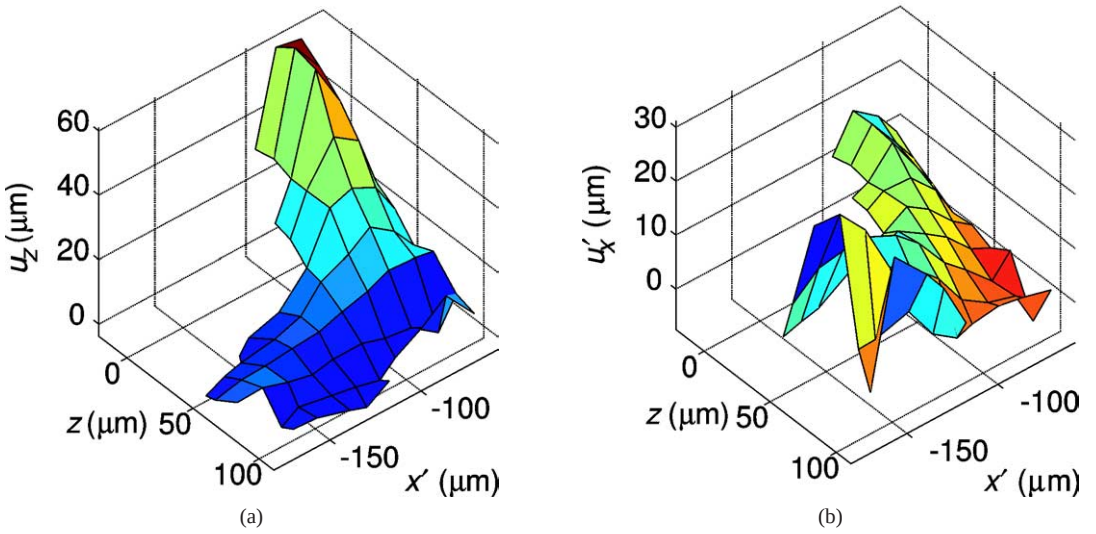

Fig. 4. Velocity fields of the BSA interior node in the $x' \times z$ plane (cf. Fig. 11b). The flow is coming from the region $z \leqslant 0$ and flowing out at $x' \leqslant -160$ μm and $z \geqslant 100$ μm. In (a) the surface velocity field in the z-direction, along gravity, is shown, and in (b) the velocity field in the x'-direction (horizontal flow direction) is shown.

In a previous publication we have investigated the effect of the film thickness, w, on the numerical simulations of the velocity fields and have developed a number of analytical approximations [18]. In particular we have shown that for thin films the direct gravitational contribution of films to foam drainage is negligible. In Appendix A we demonstrate that the film thickness will not significantly affect the velocity fields provided that $w \ll a$, a condition that is met in our experiments.

The flow fields depend on the dimensionless parameter

$$M = \mu a/\mu_s, \tag{1}$$

which we refer to as the interfacial mobility [19]. For low interfacial mobilities, $M \ll 1$, corresponding to large surface viscosities, the interfacial velocity is essentially zero, and the velocity profiles are analogous to traditional Poiseuille flow, albeit in an odd-shaped channel. On the other hand, when $M \gg 1$, corresponding to small surface viscosities, the interfaces are very mobile and, everything else being the same, a higher average velocity through the channel results. The most important parameter for interpreting the experimental results is M.

A quantitative analysis of the experimental flow fields is quite difficult, in part because we do not know the precise location of the imaging slice in the foam channel. Fig. 5 shows the cross-section of exterior and interior channels. Using the data-fitting methods described below, the cross-section of the confocal imaging parallelepiped is indicated by the dashed lines, where the rectangle's thickness corresponds to the focal depth of the imaging slice, D. We choose a local $x' \times y'$ coordinate system for the imaging rectangle. As indicated in the figure, the x'-direction indicates the width of the parallelepiped (i.e., the long dimension), and the y'-direction the depth of the parallelepiped (i.e., the short dimension).

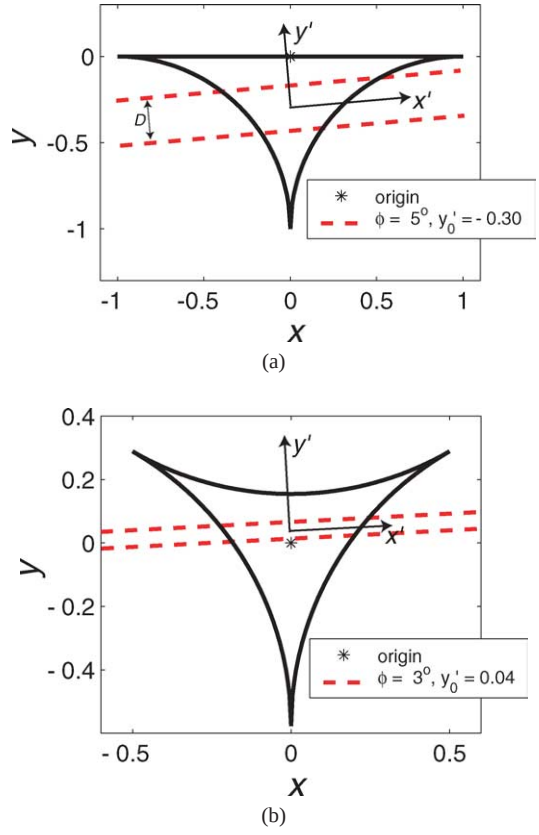

Fig. 5. Sketch of the position and orientation of the imaging slice for (a) exterior and (b) interior channels, corresponding to the exterior SDS and interior BSA channels of Table 1 and Figs. 2b and 3b. All lengths have been rescaled by a. The region between the dashed lines has thickness D, and shows the confocal imaging slice, which defines the imaging rectangle's axes, $x' \times y'$, as drawn. The flow is in the z-direction (out of the page).

The confocal slice is oriented at an angle ϕ between y-axis and y'-axis and centered about $(x = 0,\ y = y'_0)$.

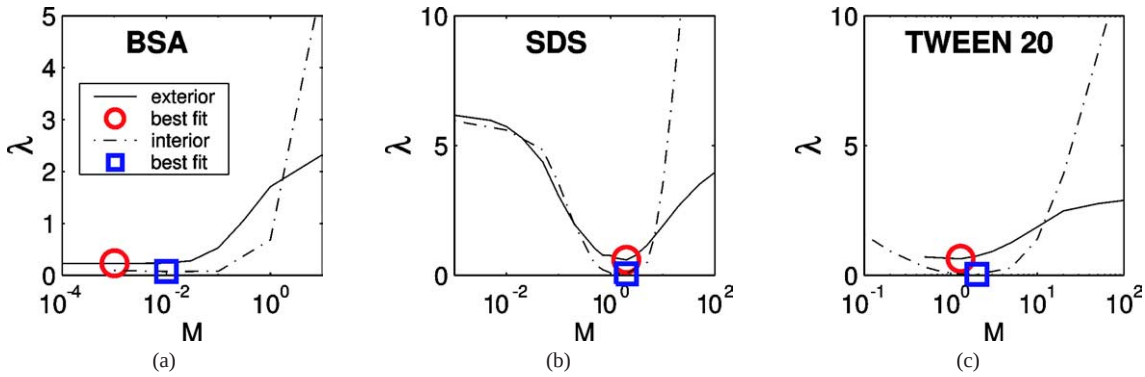

Fig. 6. The merit of fit function plotted against interfacial mobility for the interior and exterior channels of BSA, Tween 20, and SDS foams in plots (a), (b), and (c), respectively. The legend is only shown in (a). The best fit values are indicated by the symbols and given in Table 1.

In order to use numerical simulations to represent the experimental configuration for which an average velocity is measured, we need to account for the depth of the imaging slice, which is in the y' direction and, for the magnifications used in the experiments, is $D \approx 10$ μm. We perform numerical simulations, as described in earlier work [14,18], in conjunction with a probability density representative of the likelihood of actually observing a particle inside the imaging slice. Hence, we introduce a function $p(y')$ that is a maximum along the centerline of the imaging slice and goes to zero at the front and back boundaries of the imaging slice. The fitted average velocity profile along the x' direction, $u^{\text{fit}}(x')$, is an average of the simulated velocity field, $u^{\text{sim}}(x', y')$, along the y' direction, which is the depth of the imaged field,

$$u^{\text{fit}}(x') = D^{-1} \int p(y') u^{\text{sim}}(x', y')\, dy', \tag{2}$$

where we use the weighting function about the slice's center, $y' = 0$,

$$p(y') = \begin{cases} \left((D/2)^2 - y'^2\right)^{1/2} / (\pi D^2/8) & \text{for } |y'| \leqslant D/2, \\ 0 & \text{for } |y'| > D/2. \end{cases} \tag{3}$$

The best fit to the data is determined using a merit of fit function that compares the measured velocity profile across the channel, $\{x_i'^{\text{msrd}}, u_i^{\text{msrd}}\}_{i=1}^N$, consisting of N points, against the fitted velocity profile $\{x_i'^{\text{fit}}, u_i^{\text{fit}}\}_{i=1}^N$:

$$\lambda(\rho, g, \mu, D, \theta; a, y_0', \phi, M) = \frac{1}{2N} \sum_{i=1}^{N} \left(\frac{x_i'^{\text{fit}} - x_i'^{\text{msrd}}}{\sigma(x_i'^{\text{msrd}})} \right)^2 + \left(\frac{u_i^{\text{fit}} - u_i^{\text{msrd}}}{\sigma(u_i^{\text{msrd}})} \right)^2. \tag{4}$$

The arguments of λ are all of the variables that could possibly impact the velocity measurements. The first five parameters $(\rho, g, \mu, D, \theta)$ are known, and the last four parameters (a, y_0', ϕ, M) are unknown. Since we assume that the particles are uniformly distributed, the standard deviation of the averaged x-positions within a single bin is $\sigma(x_i'^{\text{msrd}}) \approx \text{binwidth}/\sqrt{12}$ [20]. The best fit to the measured velocity profile is found by discretizing the parameter space $M \times y_0' \times \phi$ and for each set of these three parameters determining the value of a which minimizes λ. The results are summarized in Table 1. The sixth row and last row report, respectively, the channel width, a, and the surface viscosity, μ_s, obtained from the fitting procedure.

Showing the dependence of the merit of fit function, λ, on the four different free parameters is difficult because the parameter space has four dimensions. Fig. 6 shows the dependence of the minimum value of λ on the interfacial mobility for interior and exterior channels of the three surfactant types. The best fit, which is the global minimum of λ, is indicated by a symbol. Both the exterior and interior SDS channels have well-defined minima at $M = \mathcal{O}(1)$, and approximate bounds for the interfacial mobility at the 70% confidence interval are $0.1 \leqslant M \leqslant 10$. For the BSA channels $M = \mathcal{O}(10^{-3})$ and approximate bounds for the interfacial mobility at the 70% confidence level are $0 \leqslant M < 1$, which is consistent with the rigid boundary condition.

In Fig. 7 we show a three-dimensional plot of the minimum value of λ in the $M \times y_0'$ plane for interior BSA, SDS, and Tween foam channels. (Recall that y_0' sets the middle of the imaging slice in the channel.) The absolute minimum, and hence best fit, is indicated by the symbol "+." Unlike the SDS and Tween channels, the merit of fit function for BSA is small for $M \lesssim 1$ and large for $M \gtrsim 1$. This is the same behavior previously seen in Fig. 6: low interfacial mobilities give better fits for protein foams, and larger interfacial mobilities, $M \approx 1$, give better fits for soap foams.

Fig. 8 shows the velocity profiles for the SDS and BSA interior channels, using the best fit parameters given in Table 1. For the BSA foam, the velocities are small at the channel's edges, indicating that the interfacial mobility is low. In contrast, for both the SDS and Tween channels, the velocities at the channel's edges are high, typically about half the maximum velocity, indicating much larger interfacial mobilities. The geometric arrangement of the confocal slice through the channel, as determined by minimizing λ, is inset into the plots. In general, the successful movies of particles were for channels with small angles of the imaging

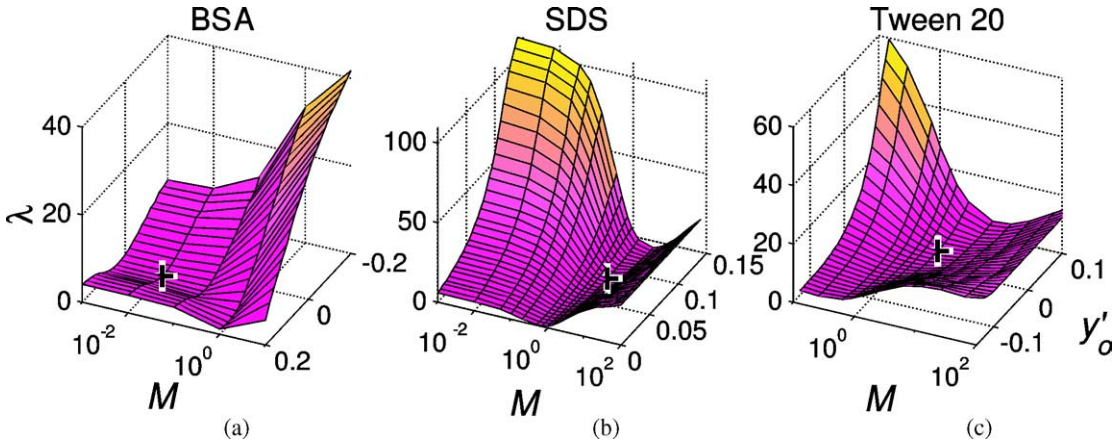

Fig. 7. The merit of fit function, λ, plotted in the $M \times y'_0$ plane for interior BSA, SDS, and Tween 20 channels. The symbol "+" denotes the global minimum of the fitting parameter space. The best fit parameters are shown in Table 1.

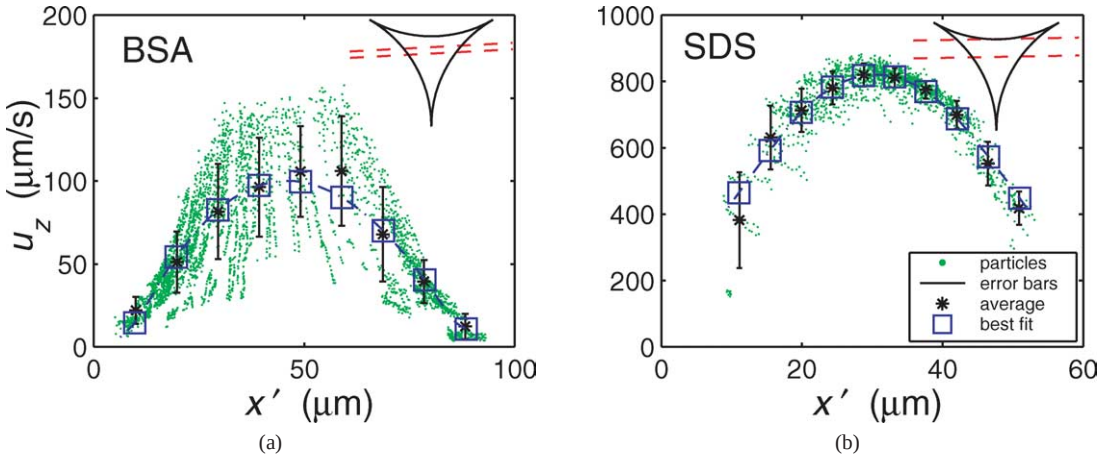

Fig. 8. Measured and fitted velocity profiles for (a) BSA and (b) SDS interior channels. The small symbols "." are the individual velocities from particle tracking; the average value is indicated by "∗" and error bars are shown. The squares connected by the dashed curve are the best fits from the theory, and these fitting parameters are given in Table 1. The insets show the geometry of the confocal slice for this fitting.

Table 1
The best fitting parameters for interior and exterior channels shown in Figs. 6–9

Surfactant	Channel type	λ	M	y'_0	a (μm)	ϕ (°)	μ_s (g/s)
BSA	Exterior	0.23	10^{-3}	−0.4	255.49	15	1.9
BSA	Interior	0.07	10^{-2}	0.0	190.41	3	0.13
SDS	Exterior	0.59	2.0	−0.3	38.07	5	1.9×10^{-5}
SDS	Interior	0.06	2.0	0.1	69.90	1	3.5×10^{-5}
Tween 20	Exterior	0.63	1.3	0.0	43.92	9	3.4×10^{-5}
Tween 20	Interior	0.03	2.0	0.0	52.91	4	2.6×10^{-5}

slice's orientation relative to the channel, i.e., small values of ϕ.

Likewise, Figs. 9a and 9b, respectively, show the velocity profiles for exterior BSA and SDS channels. Because these channels are contacting the container wall, one boundary is rigid, which diminishes the difference in overall surface mobility between the exterior protein and soap channels, as compared to the difference between interior protein and soap channels. Nonetheless, optimizing λ results in a large difference in the interfacial mobility and surface viscosity between the two protein and four soap channels—see Table 1. The surface viscosities for the SDS and Tween 20 foams are clustered about $\mu_s \approx 2 \times 10^{-5}$ g/s, and for the protein foams about $\mu_s \approx 0.5$ g/s.

We next address the issue of why the uncertainties in determining large surface viscosities from the velocity profiles are large. For small interfacial mobilities, $M \ll 1$, the velocity fields are very similar to those of channels with rigid interfaces. Neglecting the film thickness for interior channels, the maximum dimensional velocity at the surface is

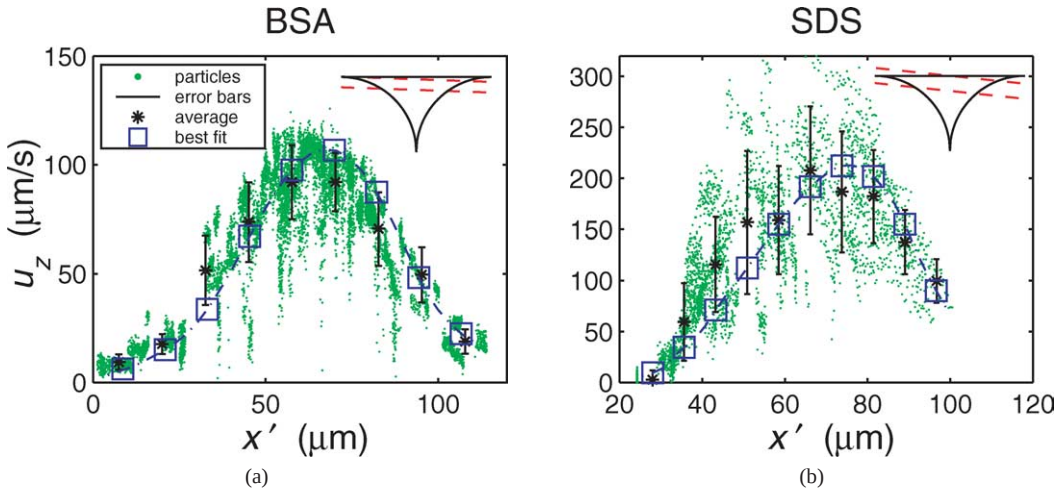

Fig. 9. Measured and fitted velocity profiles for (a) BSA and (b) SDS exterior channels. The small symbols "." are the individual velocities from particle tracking; the average value is indicated by "∗" and error bars are shown. The squares connected by the dashed curve are the best-fit velocity profiles, with the fitting parameters given in Table 1. The insets show the location for the confocal slice for these fits.

obtained from Eq. (17) in [18],

$$u_{s,\mathrm{int}} \approx \left(\frac{2\sqrt{3}-\pi}{24}\right)\left(\frac{\rho g a^2 \cos\theta}{\mu}\right)M + \mathcal{O}(M^2)$$
$$\approx 0.0134\left(\frac{\rho g a^2 \cos\theta}{\mu}\right)M + \mathcal{O}(M^2). \quad (5)$$

Likewise the maximum interfacial velocity of the exterior channels follows from Eq. (23) in [18],

$$u_{s,\mathrm{ext}} \approx 0.04\left(\frac{\rho g a^2 \cos\theta}{\mu}\right)M + \mathcal{O}(M^2). \quad (6)$$

So for small values of M, variations in the velocity field are small compared to the scatter in the velocity measurements, and thus our method for determining the surface viscosity from the velocity profiles is not very accurate. Only at larger interfacial mobilities, $M \gtrsim 1$, are there appreciable differences in the velocity fields that allow for more accurate determination of the surface viscosity.

There is some scatter in the actual data points of the velocities (see Fig. 8, for example), and we can only partially account for this scatter. The imaging slice has thickness $D \approx 10$ μm and therefore the measured velocities at a given location x' in fact are from particles that are at different depths, $y'_0 - D/2 \leqslant y' \leqslant y'_0 + D/2$ (see Fig. 5). Using the distribution function from (3), we can simulate variations in the modeled velocities as well. However the comparison between the simulated scatter and the measured scatter is not good, and typically the simulations have smaller velocity variations. We point out that for an individual particle, the variations in the measured velocity are small, typically a few percent. Thus other factors must account for the experimental scatter, such as optical distortions as the light passes through other films and Plateau borders, or perhaps a net motion of the channel, possibly due to topological rearrangements, while the confocal microscope is tracking the particles.

We next investigate the relationship between the two fitted quantities, the surface viscosity, μ_s, and the channel size, a, as summarized in Fig. 10. For SDS and Tween 20 foams, the channel widths are in the range $40 \lesssim a \lesssim 80$ μm, which is smaller than the BSA channel widths, which are $70 \lesssim a \lesssim 230$ μm. Likewise the range of the best-fit SDS surface viscosities is $2 \times 10^{-5} \lesssim \mu_s \lesssim 4 \times 10^{-5}$ g/s, which is considerably smaller than the range of the best-fit BSA surface viscosities, $10^{-3} \lesssim \mu_s \lesssim 2$ g/s [21]. This difference can be rationalized because the fluxes were roughly kept constant in the forced drainage experiments, and the velocities of the soap channels were larger than those of the protein channels. Since the liquid flux is the product of the channel's cross-section and average velocity, the SDS and Tween 20 channels are expected to be narrower than the BSA channels.

4.2. Comparison of surface viscosity with literature values

We have treated the surface viscosity as a free parameter in the analysis of the data and as a check we compare our values against those published in the literature. In general, measuring the interfacial viscosity is difficult, because its effects are very subtle, and isolating the effects of interfacial viscosity from other effects such as Marangoni stresses, Gibbs elasticity, or the viscosity of the underlying bulk fluid is complicated. We have determined the surface viscosity based upon the flow profiles, neglecting surface forces such as Marangoni stresses.

We found for SDS that there is quite a range of reported values: $10^{-5} \lesssim \mu_s \lesssim 3 \times 10^{-3}$ g/s [1,22–24]. Averaging the best-fit surface viscosities from our SDS confocal experiments gives $\langle \mu_s \rangle \approx 2.7 \times 10^{-5}$ g/s, which is on the low side, but within the literature range. For Tween 20 we obtain a similar surface viscosity $\langle \mu_s \rangle \approx 3 \times 10^{-5}$ g/s, which is not surprising because it too is a small surfactant molecule. The average surface viscosity taken from fitting the BSA veloc-

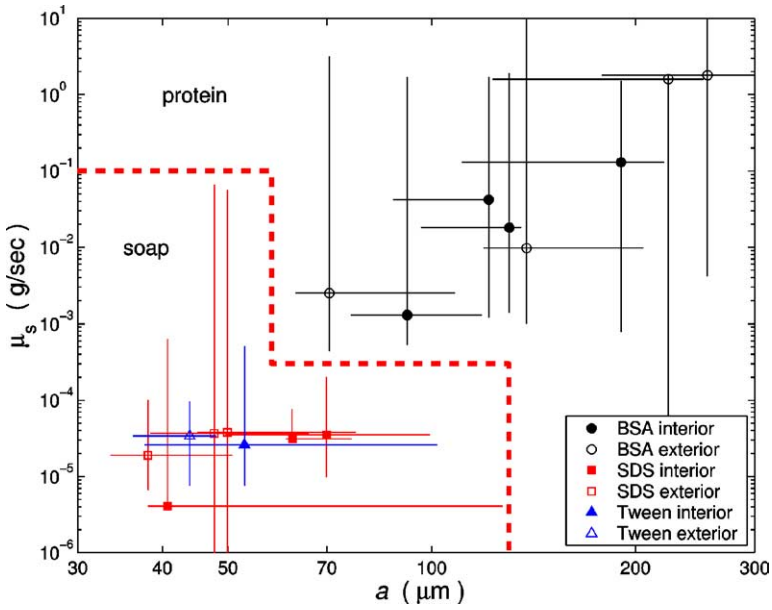

Fig. 10. Fitted surface viscosities plotted against fitted channel widths for the three types of surfactants. The solid symbols are the values obtained for interior channels, the open symbols for exterior channels, and the bars show the 70% confidence intervals for both a and μ_s. The bold dashed line demarcates the BSA foams from the SDS and Tween 20 foams.

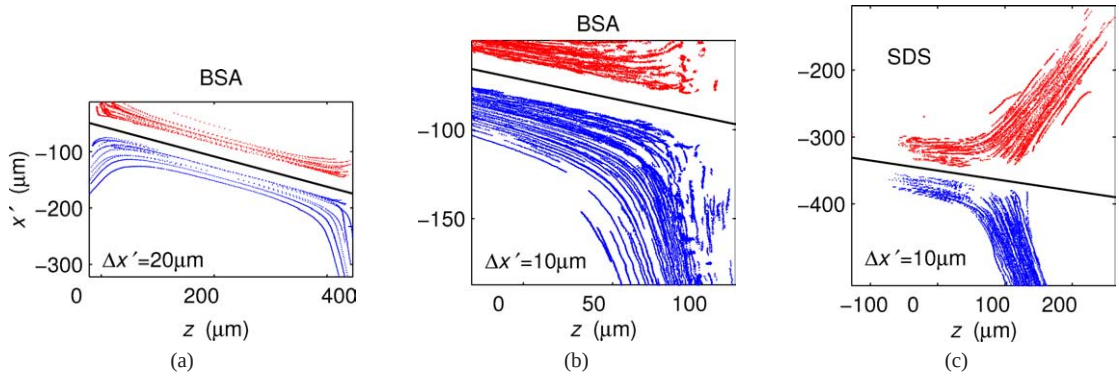

Fig. 11. Traces of particles flowing through (a), (b) interior BSA channel and node and (c) exterior SDS channel and node. For presentation purposes, the upper flow region has been displaced above the solid line by $\Delta x'$, and the lower flow region has been displaced downwards by $\Delta x'$.

ity profiles is $\langle \mu_s \rangle \approx 0.45$ g/s, which is much larger, and not unreasonable considering that protein interfaces are known to form interconnected networks.

4.3. Flow in the nodes

The confocal experiments give some insight into the qualitative features of the flow fields in the nodes. In Fig. 11 we present the particle traces whose velocity fields are shown in Fig. 4 in a different fashion. The traces are separated into two regions according to whether the particle first appears above or below the thin solid line drawn in the figure. For ease of viewing the particles in the upper region are offset by a certain amount $\Delta x'$, and particles from the lower region are offset by $-\Delta x'$. If there was mixing of the flows, then some particles originating in the upper region should move into the middle region and end up in the lower region, and vice versa. However as is readily seen from the particle traces in Fig. 11, no particles move out of their regions of origin, indicating that both in the channels and nodes there is no mixing in the direction transverse to the flow.

5. Conclusions

We have measured the velocity fields in individual Plateau borders and nodes of aqueous surfactant solutions draining through exterior and interior channels for foams made with protein surfactants as well as an ionic and a nonionic surfactant. Matching the results to theory required knowledge of bulk and surface viscosity as well as three geometric parameters (a, y_0', ϕ). We also treated the surface viscosity as an unknown parameter. The best-fit values for the surface viscosities of the soap foams were in the range of $4 \times 10^{-6} < \mu_s < 4 \times 10^{-5}$ g/s, which are in reasonable agreement with literature values. In contrast, the protein

foams had much larger surface viscosities, $10^{-3} < \mu_s < 2$ g/s. The large spread in the protein surface viscosities is due to the similarity of the flow fields for immobile interfaces, making the determination of larger surface viscosities difficult. Even under ideal conditions in the lab, determining the surface viscosity of surfactant films coating a bulk fluid is difficult, and there is quite a variation in the values of the surface viscosities determined in different labs.

The model for flow in channels is validated by the good agreement with the confocal microscopy measurements of tracer particles and good agreement of extracted surface viscosities with the literature values. Although the same modelling approach, based upon free surfactant-laden interfaces with a Newtonian surface viscosity, could be used for flow in the nodes, the actual measurements and calculations are far more challenging owing to the three-dimensional geometry involved. An estimate of the Reynolds number shows that the flow is laminar, and the data presented here indicate that there is negligible mixing in either the nodes or the channels, which is also confirmed by macroscopic experiments in foam-filled Hele–Shaw cells [25].

Aside from investigating the flow in the nodes on a more comprehensive level, other interesting questions are the effects of non-Newtonian fluids and a more realistic treatment of the surfactant-laden interfaces. Experiments with non-Newtonian fluids have shown unusual and unexplained foam drainage behavior, which must be due to microscopic details of the flow fields [26]. Furthermore, it is possible that in certain cases the interfacial rheology is not Newtonian and may exhibit shear thickening or thinning [27]. Another difficult problem is understanding the Marangoni stresses that arise from variations of the surfactant concentration at the interfaces and likely are responsible for the small observed velocities in the regions where the films are in contact with the channels [28]. The ability to experimentally access foam drainage on the microscale has opened up many possibilities for investigating microfluidics in foams, which in turn impacts our understanding of macroscopic foam drainage.

Acknowledgments

The Harvard MRSEC and the Petroleum Research Fund (Grant 35926-AC9) are acknowledged for their support, as is the Netherlands Organization for Scientific Research (NWO). We thank D. Weitz for early help with the experiments and M. Loewenberg for insightful conversations about flows induced by Marangoni forces.

Appendix A. The effect of finite film thickness on the velocity fields in channels

In order to understand the dependence of the flow fields on the multi-dimensional parameter space, we shall consider the maximum surface velocity as representative of the flow fields. For a channel inclined at an angle θ with respect to the vertical, and negligible capillary forces, the driving force for flow in the direction of the channel is gravitational: $\rho g \cos\theta$. We denote the Plateau border radius of curvature by a, the film thickness by w, the bulk viscosity by μ, and the surface viscosity by μ_s. A good approximation for the maximum surface velocity for the interior channels, $u_{\mathrm{s,int}}$, depends on the composite parameter of the interfacial mobility, Λ, and the cross-sectional area of the channel, A_{int} [18]:

$$u_{\mathrm{s,int}} \approx \frac{\rho g A_{\mathrm{int}} \cos\theta}{\mu} \sqrt{2\Lambda} \arctan\left(\sqrt{\Lambda/8}\right), \tag{A.1a}$$

where

$$A_{\mathrm{int}} = \left(\sqrt{3}\,(a+w)^2 - a^2\pi/2\right)/6 \quad \text{and} \quad \Lambda \equiv \frac{\mu a}{\mu w + \mu_s}. \tag{A.1b}$$

Similarly the maximum surface velocity for the exterior channel, $u_{\mathrm{s,ext}}$, depends on the cross-sectional area of the exterior channel that is supported by the free corner, A_{supp}, and Λ [18]:

$$u_{\mathrm{s,ext}} \approx \frac{\rho g A_{\mathrm{supp}} \cos\theta}{\mu} \sqrt{2\Lambda} \arctan\left(\sqrt{\Lambda/8}\right), \tag{A.2a}$$

where

$$A_{\mathrm{supp}} = 0.3\left\{\arctan\left(\sqrt{2}/\Lambda\right)\right\}^{1/2}\left\{(a+w)^2 - a^2\pi/4\right\}. \tag{A.2b}$$

We shall use these approximations to justify the assumption that small values for the film thickness have a negligible effect on the flow fields, upon which the present and earlier analysis of the confocal data was based [14]. For zero film thickness ($w = 0$) the interfacial mobility equals the composite parameter Λ. To first order the relative variation of the maximum surface velocity with w for an interior channel is

$$\frac{\Delta(u_{\mathrm{s,int}})}{u_{\mathrm{s,int}}(w=0)} \approx \begin{cases} \left(\frac{12}{6-\sqrt{3}\pi} - M + \mathcal{O}(M^2)\right)\left(\frac{w}{a}\right) \\ \quad \text{for } M \ll 1, \\ \left(-M/2 + \mathcal{O}(M^{1/2})\right)\left(\frac{w}{a}\right) \\ \quad \text{for } M \gg 1. \end{cases} \tag{A.3}$$

Thus the effect of the film thickness on the interior channel velocity is negligible provided that

$$\frac{w}{a} \ll \min\left\{\frac{6-\sqrt{3}\pi}{12} \approx 0.0467, 2/M\right\}. \tag{A.4}$$

For exterior channels a similar treatment shows that the variation of the maximum surface velocity is

$$\frac{\Delta(u_{\mathrm{s,ext}})}{u_{\mathrm{s,ext}}(w=0)} \approx \begin{cases} \left(9.3 - M + \mathcal{O}(M^2)\right)\left(\frac{w}{a}\right) \\ \quad \text{for } M \ll 1, \\ \left(7.7 - 0.9M^{1/2} + \mathcal{O}(M^{-1/2})\right)\left(\frac{w}{a}\right) \\ \quad \text{for } M \gg 1. \end{cases} \tag{A.5}$$

This implies that the effect of the film thickness on the exterior channel velocity is negligible provided that

$$\frac{w}{a} \ll \min\left\{\frac{1}{9.3}, (7.7 - 0.9M^{1/2})^{-1}\right\}. \tag{A.6}$$

For our microscopic experiments here, both conditions (A.4) and (A.6) are easily met. We found that $a \sim 100$ μm, and judging from the colors of the films the film thicknesses are less than a few micrometers. Carrier et al. have measured the film thickness of an aqueous foam with surfactant sodium dodecyl benzenesulfonate using an optical fiber [29] and found that the relative film thickness is small, $w/a \lesssim 10^{-2}a/L$ [30]. Thus the relative film thickness is sufficiently small to meet the condition $(w/a) \ll \min\{(6 - \sqrt{3}\pi)/12, 1/9.3\}$. Furthermore the surface mobilities for our experiments are limited; typically $M \ll 100$ and so the condition $(w/a) \ll \min\{2/M, 1/(7.7 - 0.8M^{1/2})\}$, and therefore (A.4) and (A.6), is also satisfied.

References

[1] K.J. Mysels, K. Shinoda, S. Frankel, Soap Films: Studies of Their Thinning, Pergamon, London, 1959.
[2] R.A. Leonard, R. Lemlich, AIChE J. 11 (1965) 18–24.
[3] L. Brown, G. Narsimhan, P.C. Wankat, Biotechnol. Bioengi. 36 (1990) 947–959.
[4] J.B.M. Hudales, H.N. Stein, J. Colloid Interface Sci. 140 (1990) 307–313.
[5] M.V. Ramani, R. Kumar, K.S. Gandhi, Chem. Eng. Sci. 48 (1993) 455–465.
[6] A. Bhakta, K.C. Khilar, Langmuir 7 (1991) 1827–1832.
[7] I.I. Goldfarb, K.B. Kann, I.R. Shreiber, Fluid Dynam. 23 (1988) 244–249.
[8] D. Weaire, N. Pittet, S. Hutzler, D. Pardal, Phys. Rev. Lett. 71 (1993) 2670–2673.
[9] G. Verbist, D. Weaire, A. Kraynik, J. Phys. Condens. Matter 8 (1996) 3715–3731.
[10] S.A. Koehler, S. Hilgenfeldt, H.A. Stone, Langmuir 16 (2000) 6327–6341.
[11] S.A. Koehler, S. Hilgenfeldt, H.A. Stone, Europhys. Lett. 54 (2001) 335–341.
[12] G. Brannigan, O.F.D. Bonfim, Phil. Mag. Lett. 81 (2001) 197–201.
[13] A. Saint-Jalmes, M.U. Vera, D.J. Durian, Europhys. Lett. 50 (2000) 695–701.
[14] S.A. Koehler, S. Hilgenfeldt, E.R. Weeks, H.A. Stone, Phys. Rev. E 66 (2002) 040601–040604.
[15] J.C. Crocker, D.G. Grier, J. Colloid Interface Sci. 179 (1996) 298–310.
[16] D.K. Sarkar, P.J. Wilde, Colloids Surf. B 15 (1999) 203–213.
[17] This choice of N is somewhat arbitrary; changing N does not significantly change the results provided that there are a sufficient number of particles in each bin for statistical purposes.
[18] S.A. Koehler, S. Hilgenfeldt, H.A. Stone, J. Colloid Interface Sci. 276 (2004) 420–438.
[19] The inverse of the interfacial mobility, $Bo = M^{-1}$, is known as the Boussinesq number.
[20] The factor of $\sqrt{12}$ arises from the integral $\frac{1}{a}\int_{-a/2}^{a/2} x^2\,dx = a^2/12$.
[21] Recall that for low interfacial mobilities the velocity fields are very close to the rigid boundary velocity fields—see Appendix A and Eqs. (5) and (6). Thus backing out the surface viscosity, which is the inverse of the interfacial mobility, from the measured BSA velocity profiles is difficult and will result in more scatter and larger uncertainties.
[22] D.O. Shah, N.F. Djabbarah, D.T. Wasan, Colloid Polym. Sci. 256 (1978) 1002–1008.
[23] J.T. Petkov, K.D. Danov, N.D. Denkov, R. Aust, F. Durst, Langmuir 12 (1996) 2650–2653.
[24] C. Barentin, C. Ybert, J.M. di Meglio, J.F. Joanny, J. Fluid Mech. 397 (1999) 331–349.
[25] S.A. Koehler, in preparation.
[26] M. Safouane, M. Durand, A. Saint-Jalmes, D. Langevin, V. Bergeron, J. Phys. IV 11 (2001) 275–280.
[27] C.F. Brooks, G.G. Fuller, C.W. Frank, C.R. Robertson, Langmuir 15 (1999) 2450–2459.
[28] M. Loewenberg, personal communication.
[29] V. Carrier, S. Destouesse, A. Colin, Phys. Rev. E 65 (2002) 061404.
[30] The experimental findings can be approximated as $w/\text{mm} \approx 0.25\epsilon$, and using $\epsilon \approx 0.17(a/L)^2$ and $L \approx 2.5$ mm yields the estimate $w/a \approx 10^{-2}a/L$.